# Physics, modeling, and benchmarking of ULTRARAM: A compound semiconductor-based memory device

Abhishek Kumar <sup>(1)</sup>; Musaibh Farooq Dar <sup>(1)</sup>; Peter D. Hodgson <sup>(1)</sup>; Dominic Lane <sup>(1)</sup>; Peter J. Carrington <sup>(1)</sup>; Evangelia Delli <sup>(1)</sup>; Richard Beanland <sup>(1)</sup>; Shruti Mehrotra; Manus Hayne <sup>(1)</sup>; Avirup Dasgupta <sup>∞</sup> <sup>(1)</sup>



J. Appl. Phys. 138, 095702 (2025) https://doi.org/10.1063/5.0269780





### **Articles You May Be Interested In**

Charge accumulation in GaAs/AlGaAs triple barrier resonant tunneling structures

J. Appl. Phys. (January 1998)

A method to generate additional volatile states using single-domain ferroelectric field-effect transistor

J. Appl. Phys. (April 2025)

Epitaxial GaSb films directly grown on on-axis Si(001) with low defect density by MBE

Appl. Phys. Lett. (April 2023)







## Physics, modeling, and benchmarking of ULTRARAM: A compound semiconductor-based memory device

Cite as: J. Appl. Phys. **138**, 095702 (2025); doi: 10.1063/5.0269780 Submitted: 7 March 2025 · Accepted: 31 July 2025 · Published Online: 2 September 2025







Abhishek Kumar, <sup>1</sup> Musaibh Farooq Dar, <sup>1</sup> Peter D. Hodgson, <sup>2,3</sup> Dominic Lane, <sup>2</sup> Peter J. Carrington, <sup>4</sup> Evangelia Delli, <sup>4</sup> Richard Beanland, <sup>5</sup> Shruti Mehrotra, <sup>6</sup> Manus Hayne, <sup>2,3</sup> and Avirup Dasgupta 1.a)

#### **AFFILIATIONS**

- Department of Electronics and Communication Engineering, Indian Institute of Technology Roorkee, Roorkee 247667, India
- <sup>2</sup>Department of Physics, Lancaster University, Lancaster LAI 4YB, United Kingdom
- <sup>3</sup>Quinas Technology Limited, Lancaster LA1 4YB, United Kingdom
- <sup>4</sup>School of Engineering, Lancaster University, Lancaster LAI 4YW, United Kingdom
- <sup>5</sup>Department of Physics, Warwick University, Coventry CV4 7AL, United Kingdom
- <sup>6</sup>DTE Device Modeling and CMC Lab at GlobalFoundries, Bengaluru 560045, India

a) Author to whom correspondence should be addressed: avirup@ece.iitr.ac.in

#### **ABSTRACT**

ULTRARAM is a promising emerging memory exhibiting high endurance, long retention, and ultra-low switching energy per unit area. This compound semiconductor-based non-volatile memory utilizes triple barrier resonant tunneling (TBRT) through InAs/AlSb heterostructures. In this work, we have proposed a physics-based compact model of ULTRARAM memory device that captures the real-time trapping/de-trapping of charges in the floating gate and used to calculate the device characteristics. In addition, we have performed numerical simulations of the TBRT stack using the Schrödinger equation inside the quantum well with mono-layer (~0.6 nm) variations to check the impact on memory characteristics of the device. Array-level simulations and benchmarking highlight the promise of this technology.

© 2025 Author(s). All article content, except where otherwise noted, is licensed under a Creative Commons Attribution (CC BY) license (https://creativecommons.org/licenses/by/4.0/). https://doi.org/10.1063/5.0269780

#### I. INTRODUCTION

Charge-based memories such as flash, dynamic random-access memory (DRAM), and static random-access memory (SRAM) are the primary contributors to the traditional memory market. All these technologies have limitations, though. Since it is nonvolatile, flash memory has long been the favored option for data storage. Nevertheless, because of its high voltage requirements ( $\leq$ 20 V), flash has limited endurance. DRAM uses much lower voltages and runs faster than flash, but it has reached its limits of scalability, suffers from destructive reading operations, and requires data refreshing every  $\sim$ 60 ms, which increases energy consumption and degrades performance. SRAM is the fastest among all the charge-based memories available, although even for storing a single bit of data, it requires a large physical footprint (typically six transistors).

To tackle these challenges, a novel non-volatile memory technology known as ULTRARAM has been developed. <sup>10,11</sup> Unlike traditional charge-based memories, ULTRARAM utilizes a non-classical charge-trapping mechanism, offering a unique combination of very low-energy consumption per unit area, excellent endurance, very robust non-volatility, and fast operation. To achieve these properties, ULTRARAM uses an InAs/AlSb TBRT process, explained in Sec. III. ULTRARAM integration onto Si substrates has also been demonstrated. <sup>11</sup> This is an important step toward large-scale fabrication due to superior mechanical characteristics and more environmentally sustainable production because of the plentiful supply of Si compared with group III and V elements. In this work, we have presented the device physics and a physics-based model to capture the device characteristics.

This paper is arranged to discuss the details of the ULTRARAM memory concept in Sec. II. This is followed by the TBRT physics and ULTRARAM device modeling with benchmark in Secs. III and IV, respectively. We conclude in Sec. V.

#### II. MEMORY CONCEPT

ULTRARAM is a non-conventional charge-storage nonvolatile memory (NVM) with a structure similar to flash but utilizes TBRT to achieve its remarkable properties, as shown in Fig. 1. Logic states are stored on a floating gate that is separated from the control gate (CG) by an oxide layer. The application of voltage on the CG results in the trapping of charges in the floating gate (FG) by a resonant tunneling process through the TBRT structure. The logic states (0/1) are determined by the presence/lack of charge on the FG. The non-destructive read process occurs by the application of voltage between the source (S) and drain (D). The novelty of ULTRARAM results from ultra-fast switching of the TBRT structure from a highly resistive state to a highly conductive state by applying a small voltage of  $\pm 2.5$  V. This is accomplished by careful design of the AlSb barrier and InAs quantum well (QW) layer thicknesses of the TBRT. Without applied voltage, the energy levels of the QWs reside at unusually high values, are not aligned with each other, and are well above the energy levels of the FG and channel layers, leading to a large barrier that prevents electron transfer into or out of the FG. This is a consequence of narrow QWs and the low electron-effective mass in InAs. However, the application of a positive bias to the CG tilts the conduction band in a way that the QW energy levels align with the occupied electron states in the channel, resulting in electrons flowing rapidly through the TBRT structure by intrinsically fast resonant tunneling into the FG (program). A negative bias on the CG has the equal and opposite effect (erase).

Molecular beam epitaxy was used to deposit the ULTRARAM layers on 3-in. Si n-type substrates. These substrates produce diatomic steps on the nonpolar Si surface due to their 4° offcut

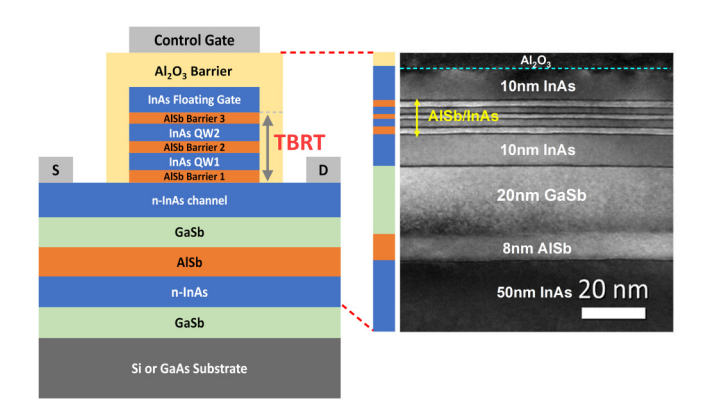
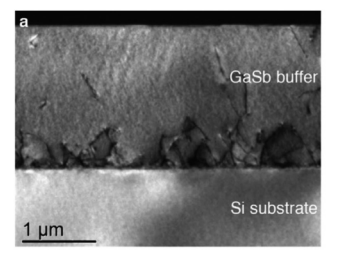
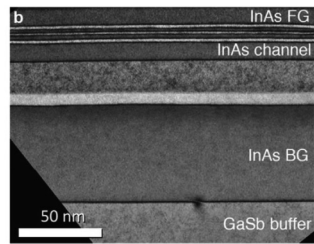


FIG. 1. Schematic of an ULTRARAM memory device and the corresponding TEM image. 10 From Lane et al., IEEE Trans. Electron Dev. 68(5), 2271-2274 (2021). Copyright 2021 Author(s), licensed under a Creative Commons Attribution 4.0 (CC BY 4.0) license.





**FIG. 2.** III–V on Si material characterization. (a) Dark-field g=220 transmission electron microscope (TEM) image of a GaSb/Si buffer layer. (b) Dark-field  $g=002\ \text{TEM}$  image of the ULTRARAM sample. 11 Only the memory layers and the top of the GaSb buffer are visible in this image. A single misfit dislocation is visible in the InAs/GaSb buffer interface. From Hodgson et al., Adv. Electron. Mater. 8(4), 2101103 (2022). Copyright 2022 Author(s), licensed under a Creative Commons Attribution 4.0 (CC BY 4.0) license.

pointing in the [011] crystal direction. 12 This feature aids in inhibiting the development of antiphase domains (APDs) in polar III-V materials as they grow. A GaSb buffer growth technique was developed in order to provide a high-quality III-V surface onto which the memory epilayers can be deposited. This was accomplished by first thermally desorbing the native oxide from the Si wafer's surface and then depositing a 17 monolayer (ML) AlSb nucleation layer, which resulted in the creation of 3D islands. <sup>13</sup> These islands facilitated 2D epitaxy and minimized planar twinning defects by shortening the diffusion length of Ga atoms when depositing the shortening the diffusion length of Ga atoms when depositing the subsequent  $2\mu$ m GaSb buffer. <sup>14</sup> An interface misfit array at the Si to III–V interface relieved the large lattice mismatch of 12.3%. <sup>15</sup> Si to III-V interface relieved the large lattice mismatch of 12.3%. 15 A two-temperature-step GaSb growth process has been utilized to reduce the density of threading dislocations that spread vertically. 16 The resulting GaSb buffer layer had a surface defect density of  $\frac{35}{5}$  (2.5 + 0.1) × 10<sup>8</sup> cm<sup>-2</sup> TRM.  $(2.5 \pm 0.1) \times 10^8 \,\mathrm{cm}^{-2}$ . TEM images in Fig. 2(a) showed that the  $^{33}$ buffer layer was APD free and the bulk of the threading dislocations was restricted to the first 500 nm of GaSb. This forms a highquality, optimal GaSb buffer layer on the Si substrate that is

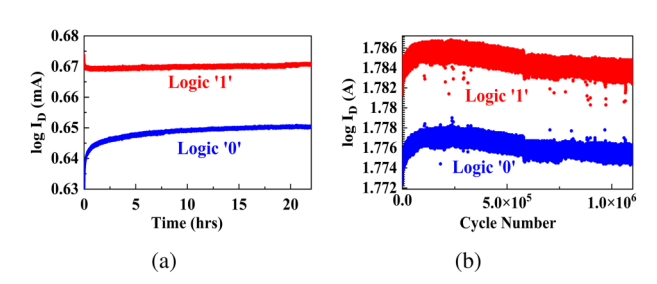


FIG. 3. (a) Room-temperature retention data. Program and erase cycles consisted of 10 ms duration pulses at  $\pm 2.5$  V. Readout is performed at an S-D bias of 0.2 V and in the absence of gate bias. (b) Endurance data for continuous program-read-erase-read cycling (5 ms pulses) on a memory cell demonstrating a clear 0/1 contrast exceeding 10<sup>6</sup> cycles<sup>11</sup> From Hodgson et al., Adv. Electron. Mater. 8(4), 2101103 (2022). Copyright 2022 Author(s), licensed under a Creative Commons Attribution 4.0 (CC BY 4.0) license.

FIG. 4. Band structures of InAs (direct bandgap) and AISb (indirect bandgap) as a function of wavevector (K).

appropriate for memory layer deposition. As seen in Fig. 2(b), the initial epilayers formed on this buffer are the 50 nm InAs n-type back gate (BG) and an 8 nm AlSb barrier layer. Next, a 20 nm GaSb spacer was deposited, followed by a 10 nm InAs n-type layer (channel) and the InAs/AlSb TBRT, which comprises 1.8 nm of AlSb, 3.0 nm of InAs, 1.2 nm of AlSb, 2.4 nm of InAs, and 1.8 nm of AlSb. Finally, the structure is completed by a 10 nm InAs FG. 10 and 20  $\mu$ m devices were then fabricated using standard cleanroom techniques. Figure 3 shows the measured retention and endurance characteristics of the ULTARAM memory cell on a Si substrate.

#### **III. TBRT PHYSICS AND MODELING**

Unlike flash, which uses a single  $SiO_2$  barrier, ULTRARAM utilizes a TBRT to store, charge, and discharge the FG. This structure provides a high-potential electron barrier ( $\sim$ 2.1 eV) with no bias and allows fast resonant tunneling at program/erase pulse ( $\pm$ 2.5 V) with switching energy per unit area 1000 times lower than flash and 100 times lower than DRAM. InAs/AlSb have been chosen as QWs and barriers, respectively, resulting in high-quality heterojunctions due to the approximately matched lattice constant (6.1 Å). Also, this combination of materials provides a large conduction band offset of 1.35 eV. However, an additional phonon interaction of 0.73 eV is required to traverse the indirect bandgap of these materials, as shown in Fig. 4. Consequently, the conduction band offset of the InAs/AlSb heterojunction forms a 2.1 eV

energy barrier for electron transport. We have performed numerical simulations of the TBRT stack using the Schrödinger equation inside the QW with mono-layer ( $\sim$ 0.6 nm) variations, <sup>17</sup> as given in Table I. Figure 5 shows the variations in the QWs and barrier thicknesses and their corresponding change in the energy levels and probability density of wave functions. Additionally, the impact of energy level changes on the current density of the TBRT stack is shown in Figs. 6(a) and 6(b), as well as the change in the memory window of the device is shown in Figs. 6(c) and 6(d). This shows notable differences when the QW widths are varied, as the changes in energy levels are significant. However, a very minute change has been seen with the change in barrier thickness, as the resonant tunneling mechanism is still the same with  $\pm 1$  ML barrier change, and the same can be observed in Fig. 5. TBRT parameters are, thus, sensitive to a 0.6 nm monolayer variation in the QWs, which would lead significant changes in the device characteristics. This highlights the requirement for precise control of QWs during fabrication, as these are more critical to stabilize the device characteristics. Further work is required to assess variations in fabrication and changes in material properties at sub-nanometer nodes.

To capture the trapping/de-trapping in the FG through the TBRT barrier, we have developed a physics-based compact model for multi-barrier resonant tunneling current.<sup>18</sup> The compact model assumes that (a) the tunneling process preserves the transverse momentum, (b) the distribution of the electric field is uniform in the structure, and (c) the effective mass approximation.<sup>19</sup> Using these, the current density can be described as <sup>18</sup>

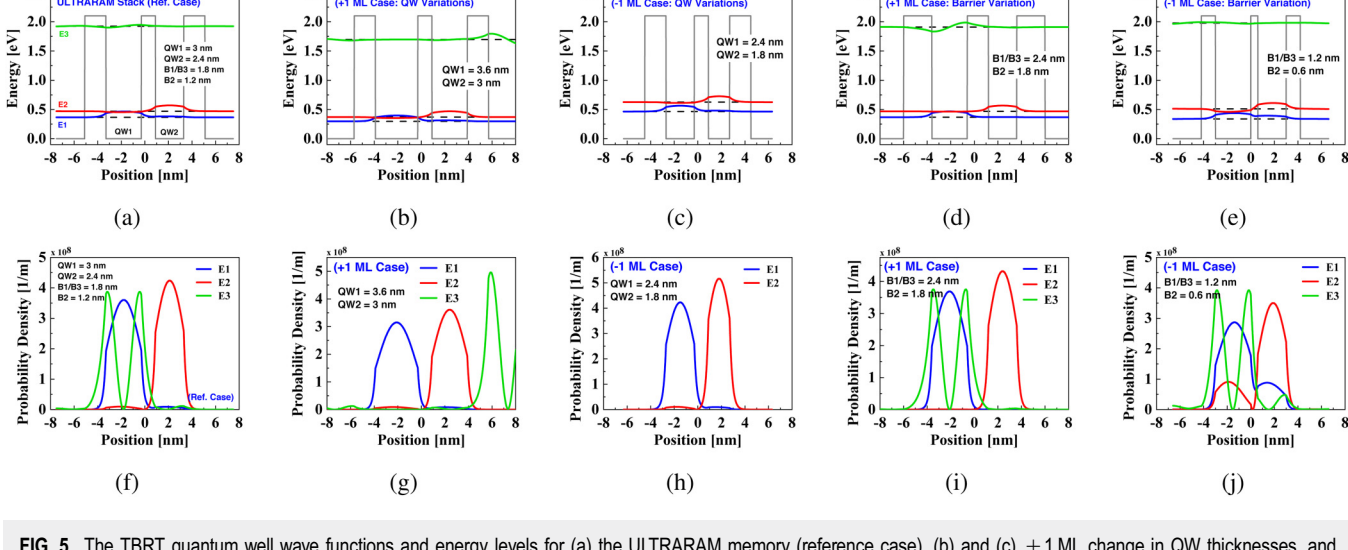
$$J = \frac{q_e m^* kT}{2\pi^2 \hbar^3} \int_0^\infty T(E_x, V) D(E_x, V) dE_x,$$
 (1)

where  $q_e$  is the charge of an electron,  $m^*$  is the effective mass of the electron, k is Boltzmann's constant, T is the absolute temperature,  $\hbar$  is reduced Planck's constant,  $E_x$  is the longitudinal energy, V is the potential applied to the structure, and  $D(E_x, V)$  is the supply function and can be given as

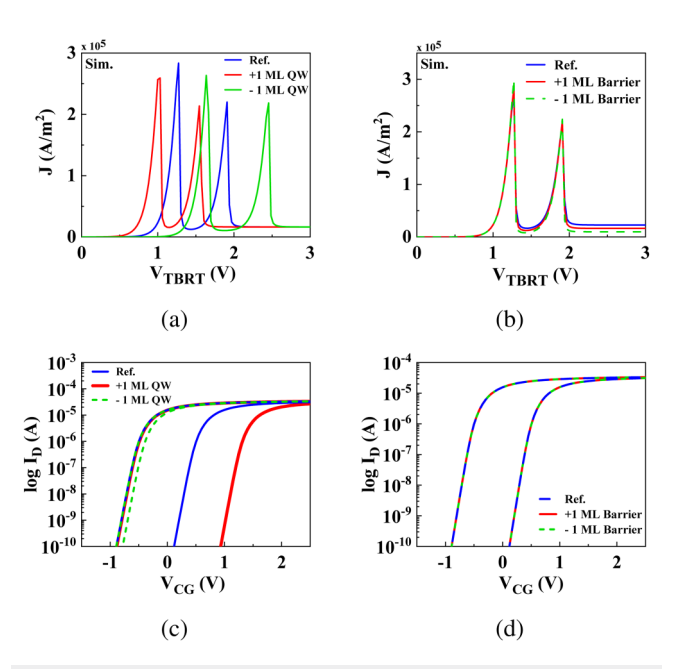
$$D(E_x, V) = ln \left[ \frac{1 + \exp(\frac{E_f - E_x}{kT})}{1 + \exp(\frac{E_f - E_x}{kT} - q_e V)} \right].$$
 (2)

TABLE I. Monolayer thickness change in TBRT stack.

ML change	AlSb B1 (nm)	InAs QW1 (nm)	AlSb B2 (nm)	InAs QW2 (nm)	AlSb B3 (nm)
Ref. layer	1.8	3.0	1.2	2.4	1.8
+1 ML QW	1.8	3.6	1.2	3.0	1.8
−1 ML QW	1.8	2.4	1.2	1.8	1.8
+1 ML barrier	2.4	3.0	1.8	2.4	2.4
−1 ML barrier	1.2	3.0	0.6	2.4	1.2



**FIG. 5.** The TBRT quantum well wave functions and energy levels for (a) the ULTRARAM memory (reference case), (b) and (c)  $\pm 1$  ML change in QW thicknesses, and (d) and (e)  $\pm 1$  ML change in barrier thicknesses. Variations in probability density (f) for ULTRARAM memory (reference case), (g) and (h)  $\pm 1$  ML change in QW thicknesses, and (i) and (j)  $\pm 1$  ML change in barrier thicknesses.



**FIG. 6.** Change in the TBRT current density with mono-layer (ML) change in (a) QWs and (b) barrier thicknesses with respect to TBRT stack voltage ( $V_{TBRT}$ ). Change in memory window of the device with a ML change in (c) QWs and (d) barrier thicknesses of TBRT stack with respect to control gate voltage ( $V_{CG}$ ). Here,  $\pm 1$  ML is the change in one lattice constant (0.6 nm) as specified in Table I.

 $T(E_x, V)$  is the tunnelling transmission coefficient approximated as <sup>19</sup>

$$T(E_x, V) = \frac{\Gamma^2}{(E_x - (E_R - q_e V n))^2 + \Gamma^2},$$
 (3)

where  $\Gamma$  is the half-width of resonance level,  $E_R$  is the energy of the resonant level relative to the bottom of the well at its center, and n is the voltage drop factor at the center of the well. For equal width barriers, n is 0.5; otherwise, it can be determined from the analysis or used as a fitting parameter.  $T(E_X, V)$  is assumed to be Lorentzian, and it is negligible if  $\Gamma$  is small compared to thermal energy (i.e.,  $E_X = E_R - q_e V n$ ). Now, solving the integration in Eq. (1) using Eqs. (2) and (3) results in the resonant tunneling current density for the double barrier and can be given as

$$J = J_0 D(E_x, V) \left[ \frac{\pi}{2} + tan^{-1} \left( \frac{E_R - q_e Vn}{\Gamma} \right) \right], \tag{4}$$

where  $J_0 = q_e m^* kT/(2\pi^2 \hbar^3)$ .

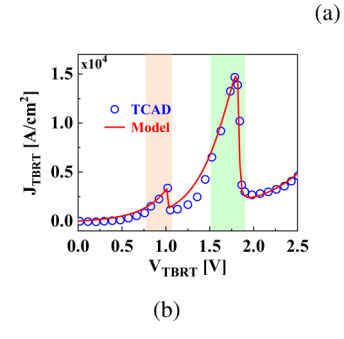
$$J_{tbrt} = J_0 ln \left[ \frac{1 + \exp(\frac{E_f - E_{R1} + q_e V n_1}{kT})}{1 + \exp(\frac{E_f - E_{R1} + q_e V (n_1 - 1)}{kT})} \right] \left[ \frac{\pi}{2} + tan^{-1} \left( \frac{E_{R1} - q_e V n_1}{\Gamma_1} \right) \right]$$

$$+ J_0 ln \left[ \frac{1 + \exp(\frac{E_f - E_{R2} + q_e V n_2}{kT})}{1 + \exp(\frac{E_f - E_{R2} + q_e V (n_2 - 1)}{kT})} \right] \left[ \frac{\pi}{2} + tan^{-1} \left( \frac{E_{R2} - q_e V n_2}{\Gamma_2} \right) \right]$$

$$+ H \left( e^{q_e V n_3 / kT} - 1 \right). \tag{5}$$







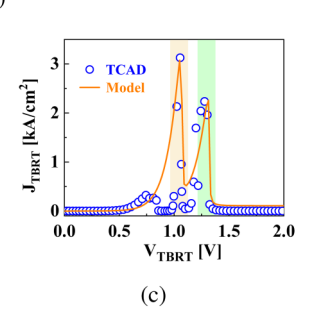


**FIG. 7.** Schematic of (a) GaAs/AlGaAs and InAs/AlSb material-based TBRT structures used for TCAD simulations. (b) and (c) Validation of the proposed model with TCAD data.

In the TBRT, there are two resonance levels. The second resonance in the TBRT can be modeled using an additional term similar to Eq. (4). This form produces the double peaks due to resonant tunneling. To capture the thermal excitation over a barrier, an additional thermionic component can be added as  $J_{th} = H(e^{eVn_3/kT}-1)$ , where H and  $n_3$  can be used as fitting parameters. Equation (5) shows the current density for the TBRT stack. This accurately captures the TBRT current density and has been validated with two different compound semiconductor-based TBRT stacks, as shown in Fig. 7.

We have simulated the TBRT structure in a commercial TCAD simulator, where the self-consistent Poisson–Schrödinger equation and the non-equilibrium Green's function (NEGF) approach are used. The NEGF model, which considers the fluctuation properties of electrons in the direction of transport and transverse, can be used to predict eigen energies, eigenfunctions, and current–voltage characteristics of the QW. In particular, we have validated the model of Eq. (5) with AlSb/InAs-based TBRT used in ULTRARAM devices, where AlSb is the barrier material and InAs is the QW. Note that there is a negligible contribution of thermionic current at room temperature.

#### IV. ULTRARAM MODEL AND BENCHMARKING

The current density from the TBRT model is further used to calculate charge trapping and de-trapping in the FG of ULTRARAM. An R-C network has been used to integrate the TBRT current over the applied input duration to obtain the real-

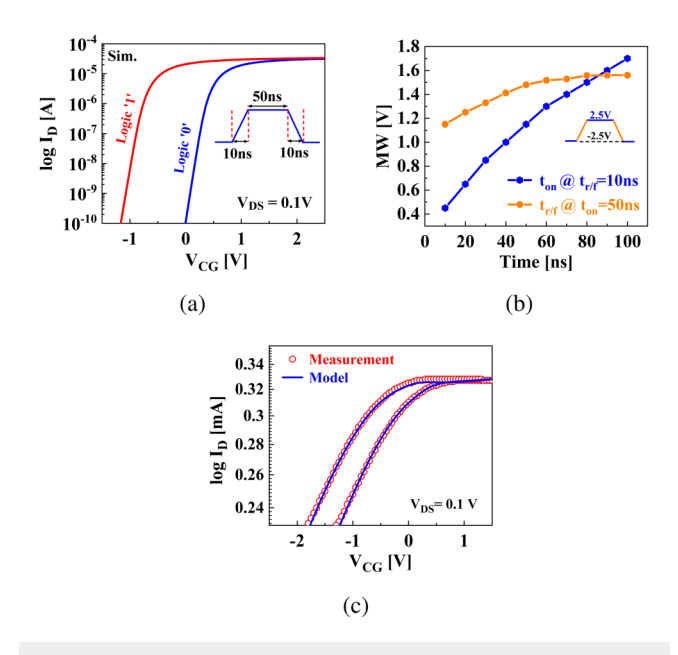


**FIG. 8.** (a) Simulated I–V with the applied input gate pulse of  $\pm 2.5$  V,  $L_g=1\,\mu\mathrm{m}$ , and  $W=1\,\mu\mathrm{m}$ . The gate capacitance  $C_{gg}\approx 7f\!/\!F$  has been calculated using the model. (b) Variations in MW of the device for pulse width  $(t_{on})$  and riselfall time  $(t_r/t_f)$  of the input gate pulse. (c) Validation of model with experimental I–V characteristics. <sup>11</sup> The following parameters have been used for calibration:  $L_g=10\,\mu\mathrm{m}$ ,  $W=17\,\mu\mathrm{m}$ , and voltage pulse of  $\pm 2.5$  V. The  $C_{gg}\approx 1.2pF$  has been calculated using the model.

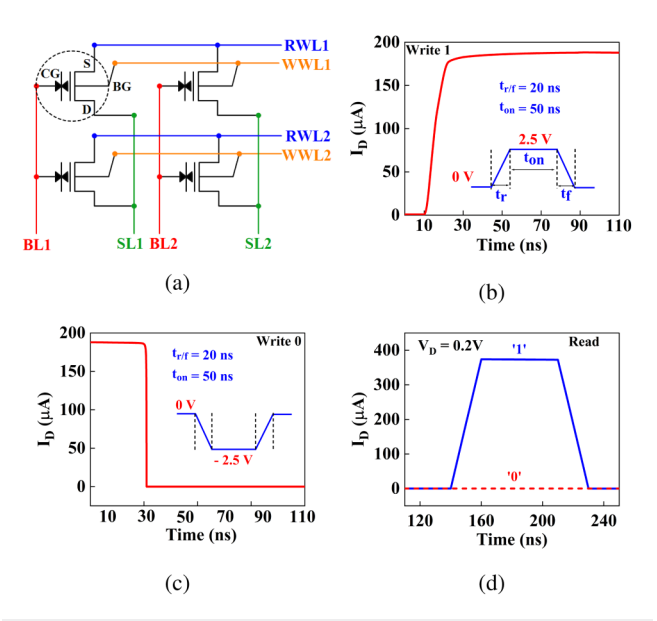


**FIG. 9.** (a)  $2\times 2$  Array with ULTRARAM memory cells, (b) Write "1" operation, (c) Write "0," and (d) Read operation.

Memory Op	eration	Write (V)	Read (V)
WWLs	Accessed	0	0
	Others	$V_{WRITE}/2$	0
RWLs	Accessed	0	$V_{\mathit{READ}}$
	Others	0	0
BLs	Accessed	$V_{WRITE}$	0
	Others	$V_{WRITE}/2$	0
SLs	Accessed	0	0
	Others	0	0

time FG charge. Furthermore, this charge is used to calculate the threshold voltage shift in the program/erase state. The drain current of the device can be expressed as

$$I_{ds} = \mu_{eff} C_g \frac{W}{L} \left( V_{gs,eff} - V_{off} - \frac{Q_{FG}}{C} - \psi_m \right) \psi_{ds}, \tag{6}$$

where  $\mu_{\it eff}$  is the effective mobility,  $C_g$  is the gate capacitance, W is the device width, L is the channel length,  $V_{gs,eff}$  is the effective applied gate voltage,  $V_{off}$  is the cut-off voltage,  $Q_{FG}$  is the charge in the FG, and  $\psi_{ds}$  is the drain to source surface potential.  $\psi_m = (\psi_s + \psi_d)/2$ , where  $\psi_s$  and  $\psi_d$  are the surface potentials at the source and drain side, respectively.  $\psi_s$  and  $\psi_d$  were calculated as given in Ref. 20.

Figure 8(a) shows the  $I_d - V_{gs}$  results simulated from the model for the programmed and erased states. The memory window (MW) depends on the input waveform, which is accurately captured in real time by the proposed model. Variation with pulse width  $(t_{on})$  and rise/fall time  $(t_{r/f})$  is shown in Fig. 8(b). We have also validated the model with experimental data of ULTRARAM, as shown in Fig. 8(c). The model shows excellent accuracy. This work focuses on demonstrating device characteristics and model validation for single-level cell operation. However, owing to ULTRARAM using a floating gate structure similar to flash, there is the possibility of controlling the amount of charge injected into the floating gate. Different numbers of charges can be stored in the floating gate by the application of gate pulses with different widths and amplitudes. This would enable the feasibility of multi-level cell operation by modulating the threshold voltage of the device in intermediate steps rather than just the two levels studied here.

A 2  $\times$  2 memory array, as shown in Fig. 9(a), is evaluated. The array includes distinct read-write paths, preventing accidental changes to stored states. Additionally, our design enables reading all cells in a column with a single cycle without scalability constraints. Moreover, the read operation is independent of the write mechanism, providing flexibility to optimize the read process for both memory and in-memory computing applications. To perform the write operation in any specific cell, the write voltage  $(V_{WRITE})$ has been applied between the control gate and back gate of the cell using the bit lines (BLs) and write word lines (WWLs). During the read operation, we apply the read voltage between the source (S) and drain (D) of the cell through the sense line (SL), maintaining the control gate voltage ( $V_{CG}$ ) at 0 V. The SL current depends on the difference in the S-D current level. To prevent any accidental write, the  $V_{SD}$  should not exceed  $V_{WRITE}/2$ . Table II shows the biasing schemes for the read and write operation for a ULTRARAM cell. Figures 9(b)-9(d) show the write 0/1 and read operation of the accessed cell. Table III shows the performance comparison of the ULTRARAM cell with other memory cells. ULTRARAM has the ability to bridge the gap between last-level cache and storage-class memories in the memory hierarchy,<sup>2</sup> owing to its latency and capacity, and can outperform NAND flash in specific areas such as speed, endurance, and energy. Therefore, it can complement NAND flash technology to achieve a better hybrid memory system with overall better performance.

Here, we have primarily focused on the device design and a physics-based compact model of single ULTRARAM cells to capture core device characteristics. However, it is understood that the real performance metrics should be judged by large array-level demonstration. We have also simulated a  $128 \times 128$  array of  $\frac{6}{57}$ ULTRARAM cells using the proposed model. A circuit-level macro-model is employed to evaluate and benchmark the on-chip learning performance in terms of area, latency, energy, and accuracy of an ULTRARAM synaptic core. It shows 91% accuracy for ULTRARAM-based CIM accelerators for VGG-8 training on the CIFAR-10 dataset, which is similar to NAND Flash-based CIM accelerators (~90%) with 5-bit weight. Full details will be disseminated in a separate article.

TABLE III. Performance metrics of ULTRARAM with other memory technologies.

Metric	SRAM <sup>21</sup>	DRAM <sup>21,22</sup>	Flash <sup>21</sup>	Fe-RAM <sup>23</sup>	STTRAM <sup>22,24</sup>	ULTRARAM (this work)
Cell area (F <sup>2</sup> )	>100	6	<4	15-35	6-50	<4
Voltage (V)	<1	<1	>10	<5	<1.5	<2.5
Switching energy (J)	$10^{-15}$	$10^{-15}$	$10^{-14}$	$10^{-11}$	$10^{-13}$	$10^{-17}$
Retention	40 ms	60 ms	>10 years	>10 years	>10 years	>1000 years
Endurance	$10^{16}$	$10^{16}$	$10^{4}$	>1010	$10^{14}$	>>10 <sup>7a</sup>
Switching time (ns)	1	10	$10^{5}$	20	~50	$\sim 100^{\rm b}$

<sup>a</sup>Experiment limited. Zero degradation observed after 10<sup>7</sup> program/erase cycles.

<sup>&</sup>lt;sup>b</sup>100 ns switching time has been observed in TCAD simulations for 20 nm channel length devices. The experimental device shows 500 μs switching time with  $20 \,\mu m$  channel length. 10

A compact model for ULTRARAM is presented providing a clear and uncomplicated physical basis for its extraordinary properties and allowing circuit-level benchmarks. The model is able to capture real-time device characteristics and shows excellent accuracy with both TCAD and measured data for TBRT and ULTRARAM, respectively. This SPICE-compatible model has been implemented in Verilog-A and is directly usable for circuit analysis.

#### **ACKNOWLEDGMENTS**

This work was supported in part by the Future Compound Semiconductor Manufacturing (Grant No. EP/P006973/1), the Horizon 2020 Framework Programme (Grant No. 777222), the Engineering and Physical Sciences Research Council (Grant No. EP/T023260/1), Innovate UK (Grant No. 10078273), the Indian Institute of Technology Roorkee, India, and the Prime Minister's Research Fellowship, Ministry of Education, Government of India (Grant No. PM-31-22-773-414).

#### **AUTHOR DECLARATIONS**

#### Conflict of Interest

The authors have no conflicts to disclose.

#### **Author Contributions**

Abhishek Kumar: Conceptualization (equal); Data curation (equal); Formal analysis (equal); Investigation Methodology (equal); Software (equal); Validation (equal); Visualization (equal); Writing - original draft (equal); Writing review & editing (equal). Musaibh Farooq Dar: Data curation (equal); Formal analysis (supporting); Software (supporting); Visualization (equal); Writing - original draft (supporting). Peter D. Hodgson: Data curation (equal); Formal analysis (equal); Investigation (equal); Project administration (equal); Supervision (equal); Validation (equal); Visualization (equal); Writing - review & editing (equal). Dominic Lane: Formal analysis (supporting); Project administration (equal); Validation (equal); Visualization (equal); Writing - review & editing (equal). Peter J. Carrington: Data curation (equal); Formal analysis (equal); Investigation (equal); Methodology (equal); Validation (equal); Visualization (equal); Writing - review & editing (equal). Evangelia Delli: Data curation (equal); Formal analysis (equal); Investigation (equal); Validation (equal); Visualization (equal); Writing - review & editing (equal). Richard Beanland: Data curation (equal); Formal analysis (equal); Funding acquisition (equal); Investigation (equal); Resources (equal); Supervision (equal); Validation (equal); Visualization (equal); Writing – review & editing (equal). **Shruti Mehrotra:** Conceptualization (equal); Data curation (equal); Formal analysis (equal); Investigation (equal); Methodology (equal); Supervision (equal); Validation (equal); Visualization (equal); Writing - review & editing (equal). Manus Hayne: Conceptualization (equal); Data curation (equal); Formal analysis (equal); Funding acquisition (equal); Investigation (equal); Methodology (equal); Project administration (equal); Supervision (equal); Validation (equal); Visualization (equal); Writing -

original draft (equal); Writing - review & editing (equal). Avirup Dasgupta: Conceptualization (equal); Data curation (equal); Formal analysis (equal); Funding acquisition (equal); Investigation (equal); Methodology (equal); Project administration (equal); Resources (equal); Software (equal); Supervision (equal); Validation (equal); Visualization (equal); Writing - original draft (equal); Writing - review & editing (equal).

#### **DATA AVAILABILITY**

The data that support the findings of this study are available within the article.

#### REFERENCES

- <sup>1</sup>A. Sebastian et al., "Memory devices and applications for in-memory computing," Nat. Nanotechnol. 15, 529-544 (2020).
- <sup>2</sup>J. S. Meena, S. M. Sze, U. Chand, and T. Y. Tseng, "Overview of emerging nonvolatile memory technologies," Nanoscale Res. Lett. 9, 1-33 (2014).
- <sup>3</sup>T. Schenk, M. Pesic, S. Slesazeck, U. Schroeder, and T. Mikolajick, "Memory technology- a primer for material scientists," Rep. Prog. Phys. 83(8), 086501
- <sup>4</sup>C. Y. Lu, K. Y. Hsieh, and R. Liu, "Future challenges of flash memory technolo-
- gies," Microelectron. Eng. **86**(3), 283–286 (2009).

  <sup>5</sup>O. Mutlu, "Memory scaling: A systems architecture perspective," in *2013 5th* IEEE International Memory Workshop, Monterey, CA, USA (IEEE, 2013),
- S. Shiratake, "Scaling and performance challenges of future DRAM," in 2020 S IEEE International Memory Workshop (IMW), Dresden, Germany (IEEE, 2020), S
- W. Mueller et al., "Challenges for the DRAM cell scaling to 40 nm," in IEEE W. Mueller et al., "Challenges for the DRAM cell scaling to 40 nm," in IEEE International Electron Devices Meeting, 2005. IEDM Technical Digest, Washington, DC, USA (IEEE, 2005), p. 4.
- 8L. Chang et al., "Stable SRAM cell design for the 32 nm node and beyond," in Digest of Technical Papers. 2005 Symposium on VLSI Technology, 2005, Kyoto, Japan (IEEE, 2005), pp. 128-129.
- M. Qazi, M. Sinangil, and A. Chandrakasan, "Challenges and directions for low-voltage SRAM," IEEE Des. Test Comput. 28(1), 32-43 (2011).
- 10 D. Lane, P. D. Hodgson, R. J. Potter, R. Beanland, and M. Hayne, "ULTRARAM: Toward the development of a III-V semiconductor, nonvolatile, random access memory," IEEE Trans. Electron Dev. 68(5), 2271-2274 (2021).
- <sup>11</sup>P. D. Hodgson, D. Lane, P. J. Carrington, E. Delli, R. Beanland, and M. Hayne, "ULTRARAM: A low-energy, high-endurance, compound-semiconductor memory on silicon," Adv. Electron. Mater. 8(4), 2101103 (2022).
- 12Y. B. Bolkhovityanov and O. P. Pchelyakov, "III-V compounds-on-Si: Heterostructure fabrication, application and prospects," Open Nanoscience J. 3(1), 20-33 (2009).
- 13S. H. Vajargah, S. Ghanad Tavakoli, J. S. Preston, R. N. Kleiman, and G. A. Botton, "Growth mechanisms of GaSb heteroepitaxial films on Si with an AlSb buffer layer," J. Appl. Phys. 114(11), 113101 (2013).
- <sup>14</sup>J. B. Rodriguez, L. Cerutti, G. Patriarche, L. Largeau, K. Madiomanana, and E. Tournie, "Characterization of antimonide based material grown by molecular epitaxy on vicinal silicon substrates via a low temperature AlSb nucleation layer," Cryst. Growth 477, 65-71 (2017).
- 15U. Serincan and B. Arpapay, "Structural and optical characterization of GaSb on Si (001) grown by molecular beam epitaxy," Semicond. Sci. Technol. 34(3),
- 16 E. Delli et al., "Heteroepitaxial integration of mid-infrared InAsSb light emitting diodes on silicon," IEEE Photonics J. 11(3), Article No. 2200608 (pp. 1-8)

- 17D. Lane and M. Hayne, "Simulations of resonant tunnelling through InAs/ AlSb heterostructures for ULTRARAM<sup>TM</sup> memory," J. Phys. D: Appl. Phys. **54**(35), 355104 (2021).
- <sup>18</sup>R. Tsu and L. Esaki, "Tunneling in a finite superlattice," Appl. Phys. Lett. 22(11), 562-564 (1973).
- <sup>19</sup>J. N. Schulman, H. J. De Los Santos, and D. H. Chow, "Physics-based RTD current-voltage equation," IEEE Electron. Dev. Lett. 17(5), 220-222
- 20<sub>S</sub>. Khandelwal, Y. S. Chauhan, and T. A. Fjeldly, "Analytical modeling of surface-potential and intrinsic charges in AlGaN/GaN HEMT devices," IEEE Trans. Electron. Dev. 59(10), 2856-2860 (2012).
- $^{\mathbf{21}}$ S. Yu and P.-Y. Chen, "Emerging memory technologies: Recent trends and prospects," IEEE Solid-State Circuits Mag. 8(2), 43-56 (2016).

- <sup>22</sup>K. Prall, "Benchmarking and metrics for emerging memory," in 2017 IEEE International Memory Workshop (IMW), Monterey, CA, USA (IEEE, 2017), pp. 1-5.
- <sup>23</sup>N. Haratipour *et al.*, "Hafnia-based FeRAM: A path toward ultra-high density for next-generation high-speed embedded memory," in 2022 International Electron Devices Meeting (IEDM), San Francisco, CA, USA (IEEE, 2022), pp. 6.7.1-6.7.4.
- <sup>24</sup>T. Y. Lee *et al.*, "World-most energy-efficient MRAM technology for nonvolatile RAM applications," in 2022 International Electron Devices Meeting (IEDM), San Francisco, CA, USA (IEEE, 2022), pp. 10.7.1-10.7.4.
- <sup>25</sup>S. Yu, Semiconductor Memory Devices and Circuits, 1st ed. (CRC Press, 2022). 26S. Lee and J. Lee, "Neuromorphic computing using NAND flash memory architecture with pulse width modulation scheme," Front. Neurosci. 14, 571292